Fluid–structure instabilities in the axial balancing system of a turbo-pump

Florian Brunier-Coulin, Nicolas Vandenberghe, Gautier Verhille, Patrice Le Gal

Fluid - Structure Instabilities in the Axial Balancing System of a Turbo-Pump

Florian Brunier-Coulin[a], Nicolas Vandenberghe[b], Gautier Verhille[b], Patrice Le Gal[b]

[a] *Aix Marseille Univ, CNRS, IUSTI, F-13013 Marseille, France*
[b] *Aix Marseille Univ, CNRS, Centrale Marseille, IRPHE, F-13013 Marseille, France*

Abstract

This article is devoted to the experimental and theoretical modeling of a fluid structure instability that affects the axial balancing system cavities of spatial turbo-pumps. After having explained the design of the laboratory experiment that mimics the real industrial set-up, we describe the observation of the instability that emerges due to the coupling of acoustic modes of a fluid cavity with the deformations of a metallic disc that closes the cavity when a flow passes through the system.

The system bifurcates towards a vibrational state via a Hopf bifurcation that can be super critical or sub critical, depending on the flow rate and inlet aperture. The experimental arrangement is fully described and tested in order to build a theoretical model that predicts very well the observed threshold of the instability.

Therefore, we expect our model to be predictive for real industrial cases.

1. Introduction

In the aerospace industry, turbo-pumps as illustrated in figure 1 (a) are equipped with very high speed rotating turbines whose rotating frequency can be as high as 100,000 rpm. Their role is to fuel the combustion chamber of the rocket engine with a high flow rate of propellant at optimized pressure. Because of the extreme hydrodynamic regimes encountered in these machines, the axial position of the rotors cannot be solely realized by mechanical components such as ball bearings. Therefore, to operate in this regime of intense mechanical loading, the force balance is ensured by the derivation of a part of the propellant flow into a cavity behind the rotor called an hydrostatic bearing or an Axial Balancing System (ABS) [2, 3]. This rotor-stator cavity is delimited radially by an inner and an outer valve positioned respectively at the periphery of the rotor and at its center. The equilibrium of dynamic pressure is responsible for the axial positioning of the rotor. However, in certain specific conditions, the response of the compressible fluid to the rotor displacements and/or deformations can lead to vibrations and instabilities. Verhille and Le Gal [4, 5] considered an ABS with a rigid and axially mobile rotor and showed the appearance of a low frequency instability where the rotor oscillates axially.

In the present study, we consider a second kind of instability involving the deformability of the rotor. So far, two kinds of instability have been observed. The first one is induced by the rotation of the disc and it involves the rotor flexibility and its coupling with the flow generated by the rotation. It has been studied in the context of high speed magnetic hard drives [6, 7]. It results in the growth of non axisymmetric deformation modes. The second instability, which is studied here, is due to the coupling between the deformations of the disc and the modulation of the pressure drop across the valve due to these deformations. This instability does not require any rotation of the disc or of the fluid and both axisymmetric and non-axisymmetric modes can be excited. In the present study we focus on the axisymmetric modes that are relevant in the context of spatial turbo-pumps. These complex interactions between hydrodynamic and solid structures may be critical for turbo-pumps. Thus, a better understanding of the fluid/structure interactions

Email address: `florian.brunier-coulin@univ-amu.fr` (Florian Brunier-Coulin)

Preprint submitted to Elsevier *January 21, 2022*

in rotor/stator systems plays a key role to improve the reliability and the performance of spatial turbo-pumps.

The paper is organised as follows. Section 2 describes the design and the characteristics of the experimental setup that allows us to investigate this instability in well controlled conditions. Then, sections 3 and 4 are devoted respectively to the full characterisation of the setup and to the description of the observed instability. To analyse this fluid/structure instability, we develop a model presented in section 5.

2. Experimental setup

2.1. Design principles

The setup under study in the present work is composed of a disk, clamped at its center, whose upper side near its outer edge is very close to an annular surface (Fig. 1). Above the disk an admission tube is used to inject air at high flow rate. After passing through the thin annular opening, the inner valve, the air flows into a cavity under the disk before going through an exit orifice. Under a given air flow, the system reaches an equilibrium state, characterised by an axisymmetric bending deformation of the disk, thus adjusting the pressure drop through the inner valve. Under some conditions the system presents an instability resulting in self sustained oscillations of the disk. Determining the conditions under which this instability occurs is the goal of the paper. Note that, in our study the disk does not rotate, as it will be shown later, the instability does not require its rotation.

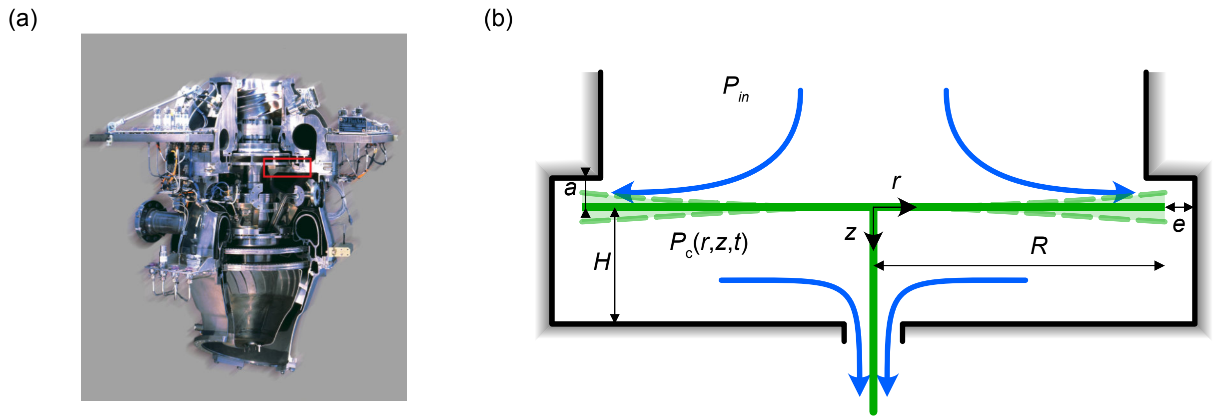

Figure 1: (a) Example of Liquid Oxygen turbo-pump with Axial Balancing System framed in red [8].(b) Simplified model of the Axial Balancing System. The flow is depicted with the blue arrows. The motion of the disk (sketched in light green) changes the gap a and thus changes the flow condition. This motion may couple with a fluctuating cavity pressure P_c thus triggering an instability.

In practice, several criteria have to be satisfied to observe the desired instability. To maximise the amplitude of the axisymetric vibration mode of the disc, it is beneficial to tune the shape and the frequency of the acoustic mode in the cavity with the ones of the normal mode of the disk. The eigenfrequencies for the acoustic cavity ω_f and for the axisymmetric bending mode of the disc ω_d are

$$\omega_f = \lambda_f \frac{c_0}{R} \tag{1}$$

$$\omega_d = \lambda_d \left(\frac{1}{R}\right)^2 \sqrt{\frac{D}{\rho_d h}} \tag{2}$$

where $D = Eh^3/12(1-\nu^2)$ is the bending modulus of the disc of thickness h, ρ_d is its density, E the Young modulus and ν the Poisson coefficient. λ_f and λ_d are two numbers that characterise the acoustic and the elastic modes. They depend on the boundary conditions in the setup. When these two frequencies are equal the thickness of the disc is given by

$$h = R\frac{\lambda_f}{\lambda_d}\frac{c_0}{c_d}\sqrt{12(1-\nu^2)}, \tag{3}$$

where c_0 is the speed of sound in the working fluid and $c_d = (E/\rho_d)^{1/2}$.

The geometry of the inner valve is also a key element in the dynamics of the system. The pressure drop across the valve can be written $\Delta P = \xi(a, Re)\rho V_0^2$ where ρ is the fluid density, V_0 is the mean velocity proportional to the flow rate Q_0 and $\xi(a, Re)$ the non-dimensional coefficient of the pressure drop that depends on the geometry of the valve and especially on the valve aperture a and on the flow conditions. As we shall see in section 5 the threshold of the instability strongly depends on the stiffness of the valve. Our setup is designed to allow for a change of the initial valve opening a_0, *i.e.* the opening at rest, without air flow. From this threshold, one can define a critical flow rate above which the system is unstable. In our facility, this critical flow rate should be lower than 11 L/s (*i.e.* 40 m^3/h) constraining the geometry of the valve.

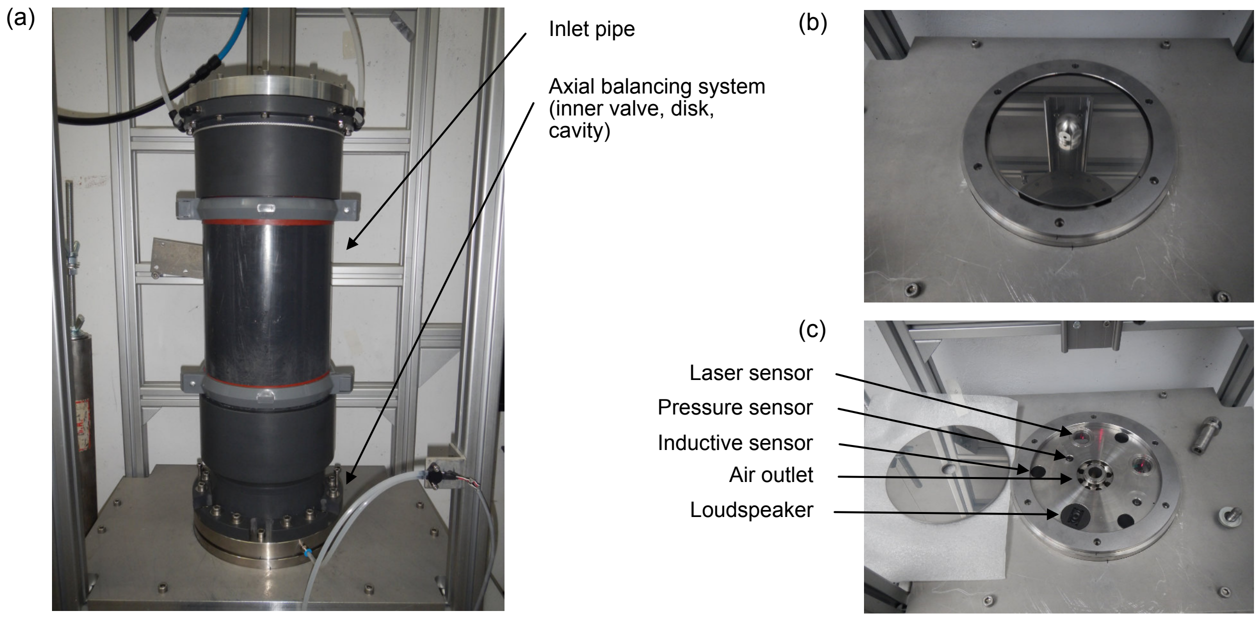

Figure 2: (a) Photograph of the setup with the 50 cm long inlet pipe having a 170 mm inner diameter. (b) Disc fixed above the cavity. The upper part of the cavity has been removed. (c) The bottom part of the cavity cavity with 3 inductive sensors, 2 laser sensors, one pressure port, 2 microphones and one loudspeaker that can be replaced by a visualisation window.

For the sake of simplicity of the experimental setup, we decide to work with air at ambient temperature. The disc is made of stainless steel with a density $\rho_d = 7700$ kg.m^{-3}, a Young modulus $E = 203$ GPa and a Poisson coefficient $\nu = 0.3$. Gravity is negligible. The radius of the disc is $R = 90$ mm and its thickness is $h = 4$ mm. The disk is held by a 300 mm in diameter hub that partially fills the acoustic cavity of height $H = 5$ mm and radius 95 mm. The walls of the cavity and the upper part of the inlet valve are made of the same steel as the disc to avoid differential thermal dilatation. Pictures of the experimental setup are shown in figure 2.

The valve aperture is controlled by a ring positioned between the bottom of the cavity and the upper part of the inlet valve. We can choose between four different rings with calibrated thicknesses of 9.00, 9.05, 9.10 and 9.15 mm and several intermediate rings made of paper with a thickness of 0.09 mm. The 9.00 mm thickness ring is used to control the initial position of the disc by imposing $a_0 = 0$ mm. The air flow enters in the cavity by the inner valve and exits to ambiant air at the center of the cavity through an annulus around the hub that is drilled by eight 10 mm diameter holes.

2.2. Instrumentation

To characterise the instability several sensors are installed on the setup to measure the different parameters. Upstream of the cavity, a flow meter (*Krohn* H250-RR) measures the flow rate crossing the cavity within the range $0.35 - 35$ m^3/h. As can be seen on the left of Figure 2, an upstream cavity (50 cm long and 170 mm in diameter) is used as a tranquillising chamber upstream the ABS cavity. The clean dry air flow crossing the cavity is provided by a compressor with a maximal pressure of 7×10^5 Pa. The flow rate is controlled by several valves which allow both a fine tuning of the desired flow rate and a short transient time to reach the stationary state. A differential pressure sensor (*NXP* MPX5500) is used to measure the pressure drop at the inlet valve within the range of 0-500 kPa, with a sensibility of 9 mV/kPa and with a response time of 1 ms. Two microphones, one omnidirectional and one unidirectional, provided by PUI Audio, are mounted flush to the cavity floor. They measure the acoustic modes within the range of 0.2-2 kHz. The vibrations of the disc are measured with two laser position sensors (*Keyence* LK-H052) located at the same radius $r = 7$ cm but separated by an angle of 90° or 135°. The acoustic modes of the cavity are initially characterised with a loud speaker K12.25 provided by *Visaton*, mounted flush on the bottom of the cavity which correspond to the stator in a rotor-stator cavity (see Figure 2 c). All the data are digitalized simultaneously at 10 kHz with a NI 6220 acquisition card.

3. Setup characterization

3.1. Characterization of bending modes and acoustic modes

Preliminary to the stability study of the axial balancing system, we perform different test to characterize the system. With the disk held in position, we proceed to ping-tests by gently tapping the disk and recording its response with the two laser vibrometers. We describe here the measurements made in the presence of the enclosure, *i.e.* in the presence of the acoustic cavity underneath the disk and of the upper surface including the inner valve upper surface.

The response of the disk to the ping test is shown in figure 3. The signal is strongly damped. The periodogram exhibits peaks at 485 Hz, 606 Hz, 740 Hz, 1576 Hz. The theoretical values [9] expected for an annular disk clamped at $r_i = 15$ mm and free at $R = 90$ mm with the material properties given in section 2.1 are 528 Hz for the mode with one Nodal Diameter (1ND), 586 Hz for the axisymmetric mode (0ND), 742 Hz for the mode 2ND and 1523 Hz for the mode 3ND showing a good agreement with the measured values. As will be discussed in details later, a key ingredient in the estimation of the instability threshold will be the damping associated with the vibration of the disk. To estimate the damping coefficient of the axisymmetric mode, we compute the Fourier spectra of the displacement signal for short subsets and then measure the decay in time of the amplitude of the 0ND mode [10] at frequency $f_0 = 606$ Hz. The results of the analysis are shown in the inset of figure 3. The exponential decay of the amplitude of the 0ND mode at short times is characterized by a decay rate $\tau_d^{-1} = 78$ s^{-1}, leading a damping coefficient $\zeta_d = \tau_d/(2\pi f_0) = 0.021$.

The ping tests have been performed with a clamping torque applied to the upper bolt holding the disk of 70 N.m. Tests have shown that if the clamping torque is lowered the damping is stronger. The value of 70 N.m was chosen to avoid possible wrapping of the disk. We attribute the unusually high value of the damping coefficient to the coupling between the disk vibration and the fluid motion in the thin gap between the disk and the upper surface (*i.e.* the inner valve). During disk vibration air has to be repetitively sucked in and expelled from the thin interval, and without the upper surface, the damping coefficient was measured lower (by a factor approximately equal to ten).

In addition, to characterize the acoustic modes of the cavity in the absence of flow, a white noise is generated by the loudspeaker and the variations of pressure in the cavity are measured by the microphone. Two main peaks have been identified in the pressure spectrum. The main one around 2330 Hz corresponds to the first azimutal mode. The second one in the range $575 - 830$ Hz corresponds to an axisymmetric mode of the cavity and is close to the first axisymmetric bending mode of the disk.

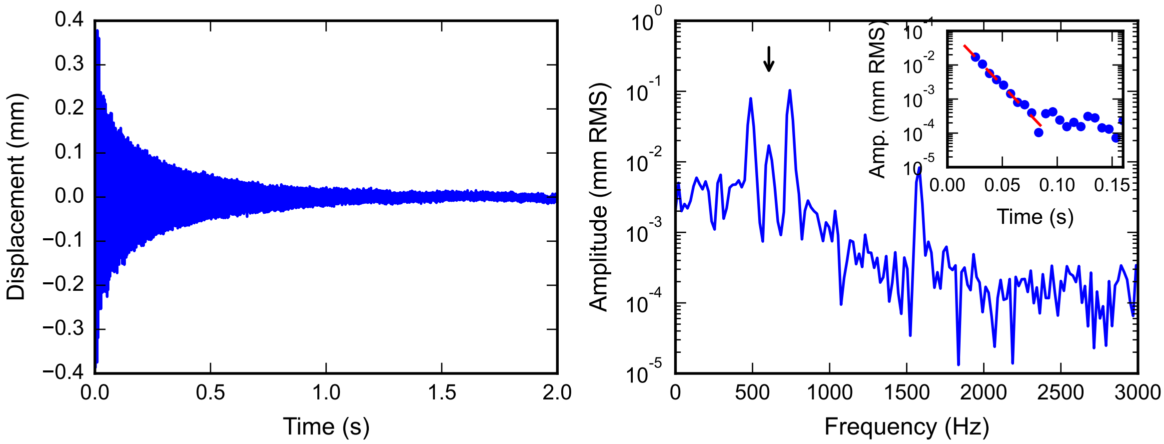

Figure 3: (a) Signal measured during a ping test by one of the laser vibrometer. (b) The periodogram of this signal (computed) between $t = 0$ and $t =$ s. The peak corresponding to the axisymmetric mode at 606 Hz is marked by an arrow. (Inset) Computing periodograms on subset of the signal of lengths 51 ms, the decay rate of the mode at 606 Hz can be determined. The red line corresponds to the exponential fit of the points above noise level. The decay rate is $\tau_d^{-1} = 78$ s^{-1}.

In presence of an air flow, acoustic modes of the tranquillising chamber are also excited. To avoid a coupling between these modes and the modes of the disc, a piece of foam in the upper half part of the pipe has been added shifting the chamber modes around 350 Hz minimizing the coupling with the bending modes.

3.2. Characterization of the inner valve

A detailed characterization of the inner valve, *i.e.* the narrow annular section through which the fluid flows into the acoustic cavity, will prove to be crucial in our analysis. In the experimental setup we record the pressure drop ΔP for different flow rates Q_0 and initial apertures a_0. The pressure drop is measured between two sensors located in the admittance chamber above the disk and in the acoustic cavity at $r = 90$ mm. As the flow rate Q_0 is increased, the pressure drop increases and the disc bends due to the pressure difference ΔP between its two sides. With the assumption of an elastic response, the transverse displacement field $u_z(r)$ is linear with the pressure difference ΔP. The solution for an annulus free at $r = R$ and clamped at $r = \alpha R$ with $\alpha < 1$ reads [11]

$$u_z(r) = \frac{\Delta P\, R^4}{64D}\left\{\frac{r^4}{R^4} - 8\frac{r^2}{R^2}\log\left(\frac{r}{R}\right) + K_1\frac{r^2}{R^2} + K_2\log\left(\frac{r}{R}\right) + K_3\right\}, \tag{4}$$

where the three constants $K_{1,2,3}$ depend on the aspect ratio α and the Poisson ratio ν and are determined using the boundary conditions (Appendix A). We assume here that the pressure in the cavity is uniform.

The measurement of the displacement $u_z(r)$ at $r = 72$ mm is in good agreement with this theory, as seen in Figure 4.a). The deviation from linear behaviour observed for $\Delta P > 4000$ Pa corresponds to an unstable regime where vibrations are observed. We can use the stationary solution 4 to compute the valve aperture $a = a_0 + u_z(R)$.

The pressure drop across the valve can be written $\Delta P = \rho_0 V_0^2 f(\alpha, Re)$, with $V_0 = Q_0/\pi R^2$ where the function f depends on the aperture $\alpha = a/R$ and on the Reynolds number $Re = aV_0/\mu$, with μ the dynamic viscosity. There is no simple way to determine the function f but correlation formula are commonly used [12]. Here we use the formula

$$\frac{\Delta P}{\rho V_0^2} = C_1\frac{C_2\alpha^{1/2} + Re}{\alpha^2 Re}, \tag{5}$$

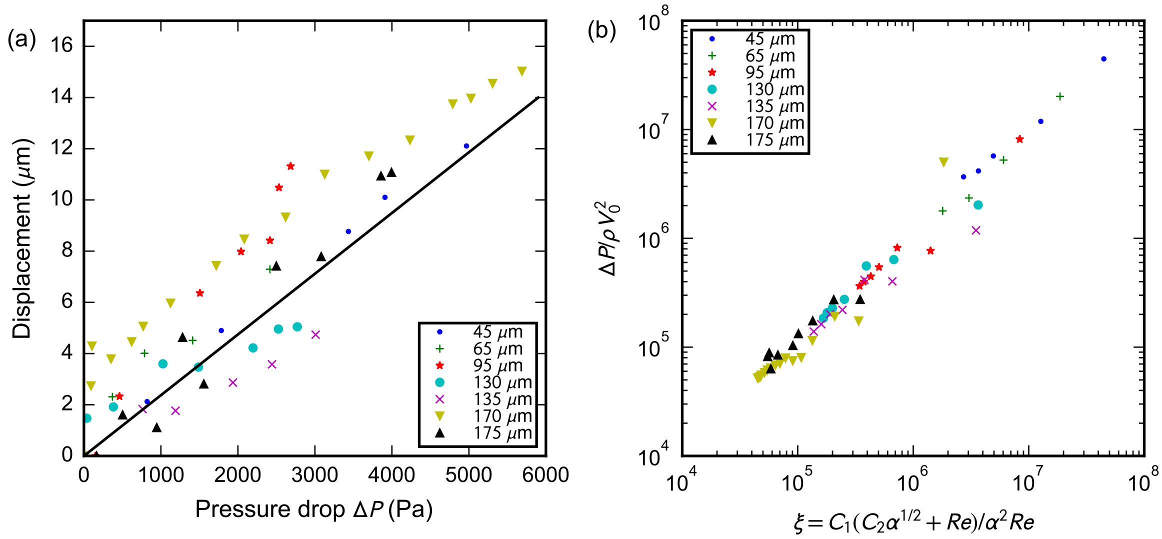

Figure 4: (a) Transverse displacement of the disc measured by the laser sensors at $r = 72$ mm as a function of the differential pressure across the inner valve for different valve apertures a_0. The blue curve represents the theoretical solution of equation 4. (b) Pressure loss across the valve $\Delta P/(\rho V_0^2)$ as a function of the non dimensional parameter of Eq.(5) with $C_1 = 0.128$ and $C_2 = 54.7$.

where $C_1 = 0.1519$ and $C_2 = 99.85$ are obtained by fitting the experimental data. Eq. (5) offers a fair description of the experimental data over the range of α and Re explored in the experiment (Fig. 4).

4. Description of the instability

4.1. Critical flow rate

Figure 5(a) presents a typical evolution of the disc vibration when the flow rate increases slowly up to values above the instability threshold. We observe a rapid increase of the amplitude of vibration when the threshold is crossed (near $t = 1$ ms). The critical flow rate is defined by the flow rate for which the amplitude of vibration is 4 times larger than the rms of the noise without flow. The evolution of the critical flow rate with the valve aperture has been investigated experimentally. It is represented in Figure 5.b) and compared with the theoretical predictions determined in section 5. This curve will be discussed in more details during the derivation of the analytical model.

As shown in figure 7.c), the frequency of the excited mode is around 610 Hz close to the threshold. This frequency and the analysis of the phase shift between the two vibration sensors evidence that the excited mode is indeed the axisymmetric bending mode.

4.2. Bifurcation

Figure 6 represents two typical evolutions of the maximum and minimum values of the transverse deformation of the disc, measured at $r = 72$ mm. For small apertures, Fig 6 (a), the behaviour is typical of a supercritical bifurcation. Below the threshold ($Q < Q_c$), vibrations are negligible. Above the threshold $Q > Q_c$, the amplitude of vibration A_{vib} increases continuously as $A_{vib} = (Q - Q_c)^{1/2}$ for $Q \gtrsim Q_c$. The oscillations are symmetrical around the equilibrium position of the disc for intermediate flow rates (here between 0.55 and 0.8 L/s). For higher flow rates, vibrations become asymmetrical when the disc comes into contact with the upper part of the cavity. This occurs when the amplitude of vibrations are greater than the mean valve aperture.

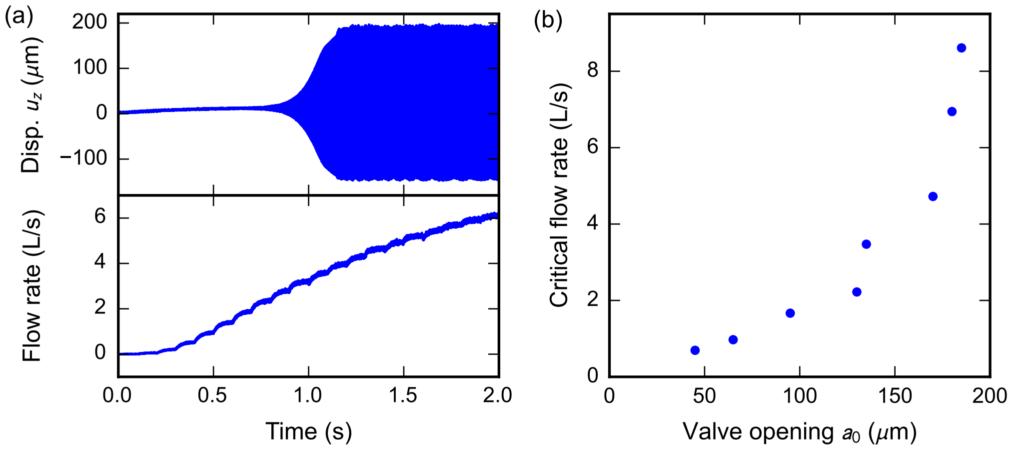

Figure 5: (a) Time evolution of the disc displacement u_z (top) measured at $r = 72$ mm and the flow rate (bottom) for an initial aperture $a_0 = 170$ μm . The amplitude of the vibrations increases when the flow rate crosses the critical flow rate (near $t = 1.0$ s). (b) Evolution of the critical flow rate as a function of the valve nominal aperture a_0.

For larger apertures, the transition becomes subcritical and a small hysteresis is observed, see Fig. 6 (b). The hysteresis is repeatable and each point represents a stationary regime.

For large apertures, for which higher flow rate can be reached before crossing the critical one, we also observe oscillations of small amplitude as shown in Fig. 6 (b). We argue that such small amplitude vibrations are induced by the turbulent flow and not the instability as they do not present the characteristic growth as it is observed in the preceding cases. They do not present the characteristic growth associated with an amplitude. A critical flow rate can still be observed. Above the threshold, the amplitude of vibration is almost six times greater than before the bifurcation and does not seem to depend on the flow rate. At this stage, the disc comes into contact with the upper part of the cavity.

The signature of a supercritical bifurcation is also observed on the growth rate of the most unstable mode. To estimate this timescale, we fit the amplitude of vibration by an exponential law $A_{vib}(t) = A_0 \exp(-t/\tau)$, as seen in Fig. 7 (a) when the flow rate varies rapidly from $Q = 0$ to $Q = Q_f$. The evolution of the growth rate $1/\tau$ is presented in Figure 7 (b). The growth rate increases first linearly with $Q_f - Q_c$ before reaching a steady value, here $\tau \simeq 26$ ms for $a_0 = 40$ μm. The saturation of the growth rate may either be due to the establishment of the flow inside the cavity or to the complete closing of the valve when the disc collides the upper part of the valve. This evolution of the growth rate is accompanied by a slight modification of the frequency of vibration, as shown on Figure 7.(c). At threshold, the pulsation is close to 610 Hz and reaches frequency as high as ~ 655 Hz for the largest flow rate.

5. Theoretical interpretation

5.1. Governing equations

To gain insight into the dynamics of the Axial Balancing System we propose here a simplified model coupling a deformable disc, an acoustic cavity and an inner valve whose aperture depends on the disc motion. We build a model taking into account these different ingredients to emphasize the key parameters in this system. The general approach used in the present study of a turbo-pump is similar to the description of wind musical instruments with vibrating reed valves such as clarinets [13, 14]. It consists in the coupling between an acoustic cavity and an elastic deformable element whose motion influences the flow in the cavity. If the general principles are similar in the two systems (wind instrument and turbo-pump) the geometry and the flow conditions are different.

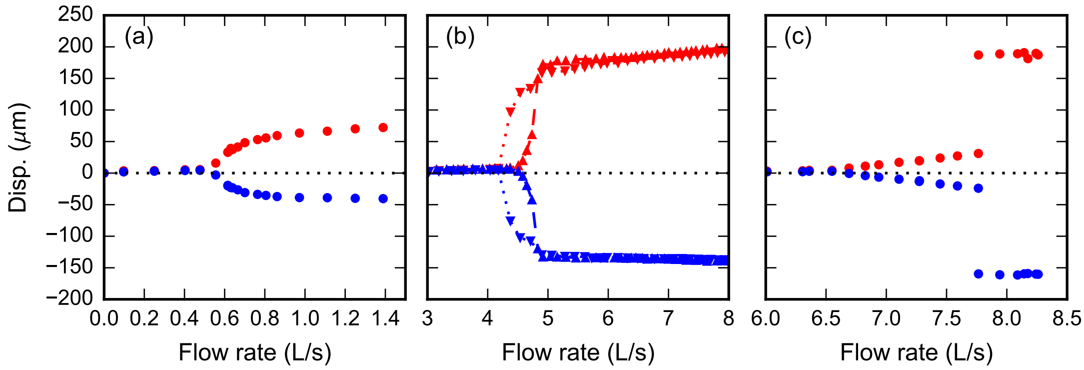

Figure 6: Evolution of the amplitude of the displacement of the disc in $r = 72$ mm as the flow rate changes. The red symbols are for the higher position of the disc (larger aperture), and the blue ones are for the lower position (smaller aperture). (a) Displacement for an initial valve aperture $a_0 = 45$ μm. A supercritical bifurcation occurs at $Q_0 \approx 0.55$ L/s. (b) Displacement for an initial valve aperture $a_0 = 170$ μm. The bifurcation is subcritical. (c) For larger initial valve aperture $a_0 = 185$ μm oscillations with limited amplitudes are observed before a sharp transition to vibration of high amplitude. The different graphs share the same scale for the displacement.

We consider a simplified model as illustrated in figure 1 (b). We approximate the Axial Balancing System as a cylindrical cavity enclosing a disc of radius R clamped in $r = 0$. The thickness of the disc h is assumed to be small enough ($h \ll R$) so that the elastic response of the plate can be described by the Kirchoff-Love elastic plate theory. Nonlinear terms will not be considered as the deformations remain small. The inner valve is characterized by its aperture, a, between the upper wall of the cavity and the disc. Cylindrical coordinates will be used and the study is restricted to axisymmetric modes.

The description of the dynamics is based on the coupling between the pressure in the lower cavity and the transverse vibrations of the disc. In the lower cavity, the fluid dynamics is described by the classical acoustic wave equation

$$\frac{1}{{c_0}^2}\frac{\partial^2 \vec{v}}{\partial t^2} - \Delta \vec{v} = 0, \tag{6}$$

where $\vec{v}$ is the velocity field and c_0 is the speed of sound. The acoustic modes are coupled with the deformation of the disc through the boundary condition as discussed later.

The vibrations of the disc are described by the bending wave equation with a forcing coming from the differential pressure acting on each face of the disc [15]

$$m_s \frac{\partial^2 u_z}{\partial t^2} + D\nabla^4 u_z = P_{in} - P_c \tag{7}$$

where u_z is the local displacement in the axial direction, P_{in} is the constant and uniform pressure above the disc, P_c is the pressure field in the cavity at the boundary of the disk, which depends on the fluid velocity $\vec{v}$, see figure 1.b). $m_s = \rho_d h$ and $D = Eh^3/12(1-\nu^2)$ are respectively the surface density and the bending modulus of the disc where ρ_d is the density, E the Young modulus and ν the Poisson coefficient. We note that we do not consider the radial deformation of the disc nor the centrifugal force that may be relevant for a disc rotating at high speeds. They are not relevant in our experimental setup. Moreover, the gravitational force is neglected in this study as it is much smaller than the pressure force $(P_{in} - P_c)S$ where S is the surface of the disc.

The inner valve controls the pressure drop $\Delta P = P_{in} - P_c(R)$ according to Eq. (5). The pressure drop across the valve thus relates the flow rate and the pressure in the cavity and it depends on the deformation of the disc through the variable $a = a_0 + u_z(R)$.

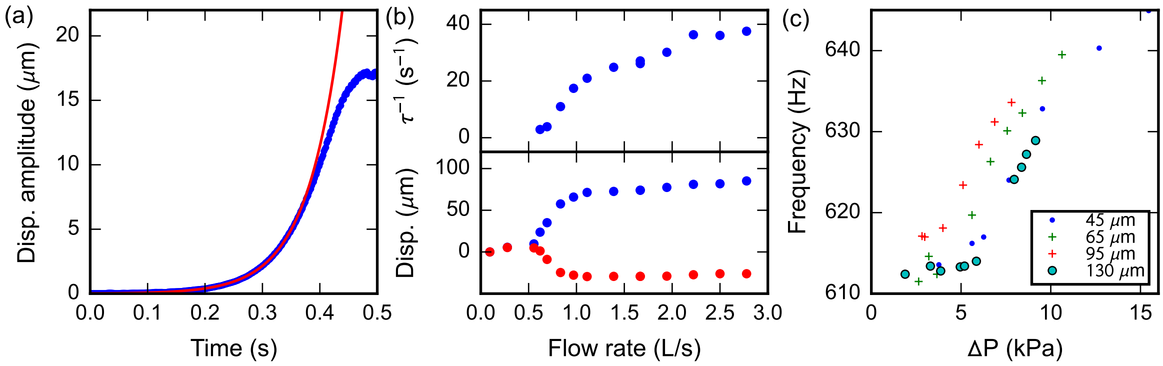

Figure 7: (a) Evolution of the amplitude of the vibrations as a function of time after a fast flow increment from 0 to 9.72 L/s with $a_0 = 170$ μm (blue circles). The red curve represents the fit by the exponential function. (b)$1/\tau$ (top) and minimal and maximal displacement of the disc in $r = 72$ mm (bottom) as a function of the flow rate Q_f for $a_0 = 45$ μm. (c) Evolution of the measured frequency with the differential pressure accross the inner valve.

5.2. Single mode oscillations of the disc

The general form of the equation for the disc (7) must be solved with the space dependent pressure P_c. To obtain a simplified system we use an energetic formulation. The kinetic energy of the disc writes

$$\mathcal{K} = \frac{1}{2}\int_0^R m_s \left(\frac{\partial u_z}{\partial t}\right)^2 2\pi r dr \tag{8}$$

The potential elastic energy for the bending disc writes

$$\mathcal{V} = \frac{1}{2}\int_0^R D\left[\left(\frac{\partial^2 u_z}{\partial r^2} + \frac{1}{r}\frac{\partial u_z}{\partial r}\right)^2 - 2(1-\nu)\frac{\partial^2 u_z}{\partial r^2}\left(\frac{1}{r}\frac{\partial u_z}{\partial r}\right)\right] 2\pi r dr \tag{9}$$

The work of pressure forces writes

$$\mathcal{W} = \int_0^R (P_{in} - P_c) u_z 2\pi r dr \tag{10}$$

It is customary to obtain an approximate formulation amenable to numerical resolution by introducing an ansatz for the displacement field of the form $u_z(r,t) = \sum a_k(t)\phi_k(r)$ where the ϕ_k are a given set of linearly independent approximation functions (see e.g. [16]). In the present work we use the simplest form of this approach and we focus on a simple form

$$u_z(r,t) = w(t)\left(\frac{r}{R}\right)^2 \tag{11}$$

This form provides a simple approximation for the first mode of the disc (though it does not verify the boundary conditions – free moment and free shear force – at $r = R$). Using this form and performing the derivative yields an equation

$$m\ddot{w} + kw = P_{in} - P_{eff} \tag{12}$$

with

$$m = 2m_s/3, \quad k = 16D(1+\nu)/R^4$$

and an effective pressure

$$P_{eff} = \frac{2}{\pi R^2}\int_0^R P_c(r)\left(\frac{r}{R}\right)^2 2\pi r dr \tag{13}$$

We note here that this approach does not take into account dissipation that will be heuristically incorporated later. We note also that this simplified approach predicts a free vibration eigenfrequency $\omega_{app} = (D/\mu R^4)^{1/2}[24(1+\nu)]^{1/2} \approx 5.58(D/\mu R^4)^{1/2}$ while the exact analytic solution, yields $\omega \approx 3.752(D/\mu R^4)^{1/2}$ [9].

To explore the possibility of an instability developing in the Axial Balancing System we consider the sum between a stationary state, called "reference state" hereafter, and a random perturbation with a zero mean materialized by a tild over the variable (see *e.g.* [1]).

5.3. Reference state

To explore the possibility of an instability developing in the Axial Balancing System, we consider a stationary state we first consider the stationary state associated with a constant flow rate $Q_0 = \pi R^2 V_0$. The flow in the cavity is then obtained from the continuity equation

$$v_r(r) = V_R \frac{R}{r} = \frac{Q_0}{2\pi H r} = V_0 \frac{R^2}{2Hr} \tag{14}$$

with $V_R = Q_0/(2\pi R H)$. We have assumed that the small deflection of the disc is negligible compared to H. The pressure field in the lower cavity is given by Bernoulli's relation

$$P_0(r) - P_0(R) = \frac{1}{2}\rho_0 V_R^2 \left[1 - (R/r)^2\right] \tag{15}$$

The pressure field can be used to compute the effective pressure from eq. (13)

$$P_{eff} = P_0(R) - \frac{1}{2}\rho_0 V_R^2 = P_0(R) - \frac{1}{2}\rho_0 V_0^2 \left(\frac{R}{2H}\right)^2 \tag{16}$$

To close the system we use the characteristic equation of the inner valve (eq. 5)

$$\Delta P_0 = P_{in} - P_0(R) = \rho_0 V_0^2 C_1 \frac{C_2 \alpha_0^{1/2} + Re_0}{\alpha_0^2 Re_0} \tag{17}$$

where $\alpha_0 = (a_0 + w_0)/R$ and $Re_0 = \rho_0 V_0 (a_0 + w_0)/\mu$ yielding an equation for the displacement in the reference state w_0

$$k w_0 = P_{in} - P_0(R) + \frac{1}{2}\rho_0 V_R^2 = \rho_0 V_0^2 \left\{ C_1 \frac{C_2 \alpha_0^{1/2} + Re_0}{\alpha_0^2 Re_0} + \frac{1}{2}\left(\frac{R}{2H}\right)^2 \right\} \tag{18}$$

We note that the second term in the brace is negligible compared to the first one.

The value of w_0 can be computed from this equation for a given set of parameters. The result is shown in figure 8, together with experimental measurements. Despite the simplifying hypotheses, the agreement between theory and the measurements is good. We note that for small values of V_0, an asymptotic solution at leading order in V_0 writes $w_0 \sim C_1 C_2 \mu V_0/(k a_0)(R/a_0)^{3/2}$

5.4. Stability analysis

The experiment is characterized by the appearance of self sustained oscillations as the flow rate reaches a critical value. To study the threshold we perform here a perturbation analysis of the reference state. A perturbation of the system is added on the stationary state calculated earlier:

$$\begin{aligned} w(t) &= w_0 + \tilde{w}(t) && (19)\\ Q(t) &= \pi R^2 V_0 + \tilde{Q}(t) && (20)\\ P_c(r,t) &= P_0(r) + \tilde{P}_c(r,t) && (21) \end{aligned}$$

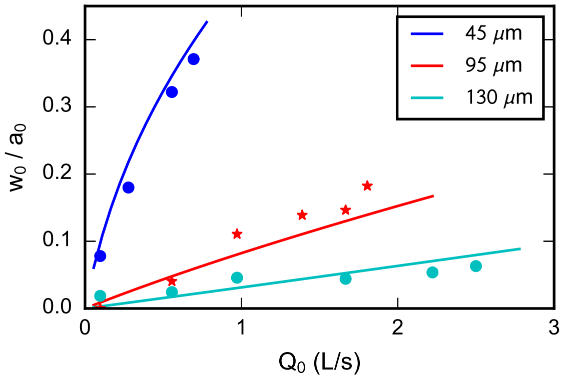

Figure 8: The displacement of the disc w_0 in the reference state for different values of the initial opening a_0. The solid lines show the solutions of eq. (18) and the dots show experimental measurements (note that the measured displacements are multiplied by $(9/7)^2$ because measurements were performed at $r = 72$ mm and not at the outer edge $R = 90$ mm. See also eq. 11). For the computations we use the geometry and the material properties for the disk given in the text (section 2) and for the fluid $\rho_0 = 1.29$ kg m^{-3}, $\mu = 18.1 \times 10^{-6}$ Pa s.

The dynamics of the disk is given by the relation deduced from eq. (12)

$$\ddot{\tilde{w}} + 2\zeta_d \omega_d \dot{\tilde{w}} + \omega_d^2 \tilde{w} = -\frac{1}{m} \tilde{P_{eff}} \tag{22}$$

where $\omega_d = (k/m)^{1/2}$. The damping term $2\zeta_d \omega_d \dot{\tilde{w}}$ is not present in eq. (12). We introduce it to account for the damping of the vibrations of the disk. The damping coefficient ζ_d can be deduced directly from the estimation of the damping of the vibrations of the disk presented in section 3.2 and in Fig. 3.

To allow for a better understanding of the stability of the system, we adopt a simple model for the acoustic cavity. We consider that the cavity behaves like an acoustic resonator near the first eigenfrequency. The derivation of the model is detailed in Appendix B and in this section we use the following form to describe the cavity near its resonance

$$\ddot{\tilde{P}}_R + 2\zeta_c \omega_c \dot{\tilde{P}}_R + \omega_c^2 \tilde{P}_R = Z_0 \frac{1}{\tau_c} \dot{\tilde{Q}} \tag{23}$$

where $\tilde{P}_R(t) = \tilde{P}_c(R,t)$ and $Z_0 = \rho_0 c_0/(\pi R^2)$ is the acoustic impedance associated with the cavity. The resonator is characterized by its eigenfrequency ω_c whose values is typically a constant of order 1 times the characteristic frequency c/R, by a damping coefficient ζ_c that depends on the exit condition, and by a time constant τ_c that characterizes the stiffness of the cavity. The different parameters depend on the geometry of the cavity and can be determined by using the method of Appendix B. In addition to this relation we assume that in the regime under study, the effective pressure is related to the pressure at $r = R$ by a linear relationship $\tilde{P_{eff}} = \gamma \tilde{P}_R$. The value of γ is also an outcome of the analysis of Appendix B.

Finally the behaviour of the inner valve is linearised. Starting from eq. (5) a linear relationship between the pressure perturbation at the exit of the inner valve $\tilde{P}_R = \tilde{P}_c(R,t)$, the perturbation flow rate $\tilde{Q}$ and the perturbation of the position $\tilde{w}$ reads

$$\tilde{Q} = -A\tilde{P}_R + B\tilde{w} \tag{24}$$

where

$$A = \frac{\pi R^2}{\rho_0 V_0} \frac{Re_0\, \alpha_0^2}{C_1 \left(2Re_0 + C_2\, \alpha_0^{1/2}\right)} \quad \text{and} \quad B = \pi R V_0 \frac{4Re_0 + 5C_2\, \alpha_0^2}{2\alpha_0 \left(2Re_0 + C_2\, \alpha_0^{1/2}\right)} \tag{25}$$

A and B vary with the imposed flow rate $Q_0 = \pi R^2 V_0$. In the limit of small flow rate ($Q_0 \to 0$),

$$A \approx \pi a_0^{5/2} R^{1/2}/(C_1 C_2 \mu), \quad B \approx 5\pi R^2 V_0/(2a_0) \tag{26}$$

Using Eq. (24), the system formed by Eqs. (22) and (23) has two unknown variables, $\tilde{w}(t)$ and $\tilde{P_R}(t)$. To study the stability of the reference state, we look for solutions of the form $\left(\tilde{w}(t), \tilde{P_R}(t)\right) = \left(\hat{w}, \hat{P_R}\right)\exp(st)$. The growth rate s is then given by the characteristic equation

$$s^4 + A_2 s^3 + A_3 s^2 + A_4 s + A_5 = 0 \tag{27}$$

where

$$\begin{aligned}
A_2 &= 2\zeta_c\omega_c + 2\zeta_d\omega_d + \frac{AZ_0}{\tau_c} \\
A_3 &= \omega_c^2 + \omega_d^2 + 2\zeta_d\omega_d\left(2\zeta_c\omega_c + \frac{AZ_0}{\tau_c}\right) \\
A_4 &= 2\zeta_d\omega_d\omega_c^2 + \omega_d^2\left(2\zeta_c\omega_c + \frac{AZ_0}{\tau_c}\right) + \frac{B\,Z_0\gamma}{m\tau_c} \\
A_5 &= \omega_c^2\omega_d^2
\end{aligned}$$

All the coefficients A_i are positive. When $Q_0 = 0$, B is zero and the two damped oscillators described by Eqns (22) and (23) are not coupled. The polynomial has four complex roots, conjugate by pairs with negative real parts. We assume here that the damping coefficients are not too high, a condition fulfilled in the experiment (otherwise real negative eigenvalues may be obtained).

As Q_0 increases, the eigenvalues move (continuously). The solution can become unstable when two complex eigenvalues cross the imaginary axis with a non-zero imaginary part (a single real eigenvalue crossing in zero is not possible because $A_5 > 0$). The evolution of the real and imaginary parts of the eigenvalues is shown in figure 9 for a set of parameters deduced from the experiment.

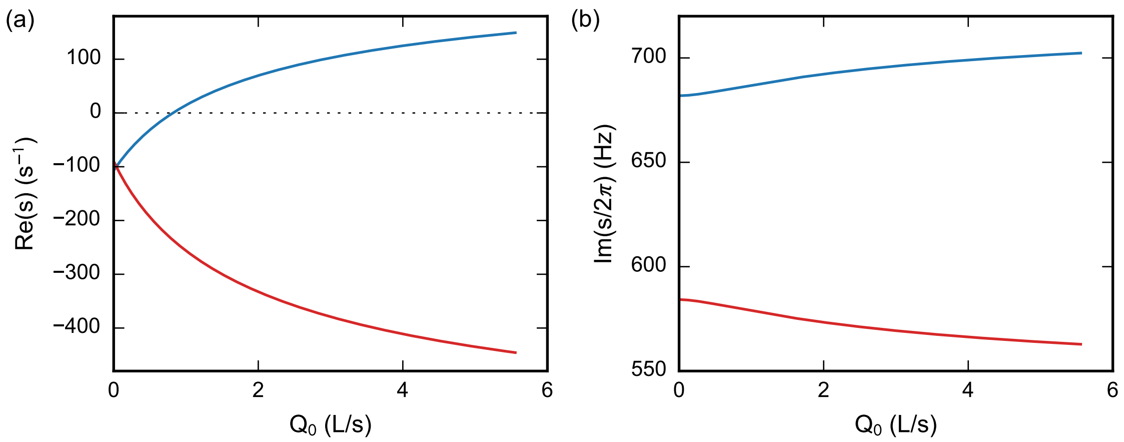

Figure 9: Evolution of the real and imaginary parts of the eigenvalues (solutions of Eq. 27). The system is stable for low flow rates with four complex eigenvalues (conjugate by pair) with negative real parts. As the flow rate increases a pair of eigenvalues crosses the imaginary axis. For the figure the geometrical parameters and material properties of section 2 are used with the properties of the cavity obtained in Appendix B and given in figure B.11. The damping coefficient of the disk is $\eta_d = 0.025$ and the initial aperture is $a_0 = 50\ \mu$m.

It is then straightforward to show (Appendix C) that the stability is maintained when

$$\mathcal{S} = A_2A_3A_4 - A_4^2 - A_5A_2^2 < 0 \tag{28}$$

The different terms that appear in the stability equation evolve when Q_0 changes. Eq. (28) presents a complicated variation with the different physical parameters and it is not easy to extract a general relation for the critical flow rate for a given set of parameters. However, using the physical parameters of the experiment, it is possible to determine the value of the critical flow rate for each value of the initial valve aperture a_0. In figure 10 we present a stability boundary in the plane (a_0, Q_0). The system is unstable above the stability threshold. The theoretical value is compared with the measurements and it shows a good agreement for the measured value of the structural damping ζ_d.

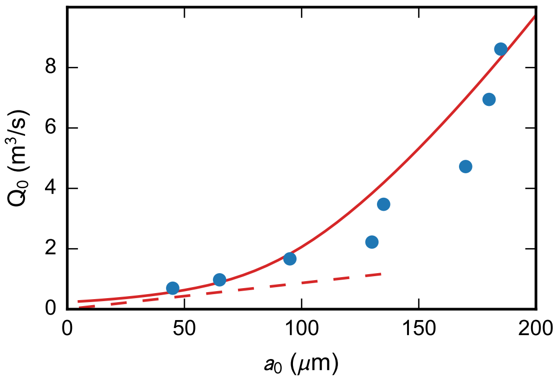

Figure 10: Stability threshold for the Axial Balancing System (solid line) obtained from Eq. (28). Above the critical flow rate Q_0 the system is unstable. The boundary is computed for the parameters of section 2 and the properties of the cavity obtained in Appendix B and given in figure B.11. The damping coefficient of the disk is $\zeta_d = 0.021$, the dots represent the critical flow rates measured in the experiment and the dashed line shows the approximate solution of Eq. (32).

5.5. Approximate stability boundary

Finally it is worth examining a simplified situation. Using the approximations for small flow rates given in Eq. (26), the stability variable $\mathcal{S}$ takes a simpler form. This approach emphasizes the importance of the valve stiffness $B = \partial Q/\partial w$ that triggers the instability through the term A_4^2 in Eq. (28). With the approximations of Eq. (26), A does not change with the flow rate and we define

$$\zeta_c' = \zeta_c + \frac{AZ_0}{2\tau_c\omega_c}$$

A_4 is the only variable varying with Q_0 and the stability equation can be written

$$-A_4^2 + A_2A_3A_4 - A_5A_2^2 = 0 \tag{29}$$

with an associated solution

$$A_4 = \frac{A_2}{2}\left(A_3 + \sqrt{A_3^2 - 4A_5}\right) \tag{30}$$

The other solution (with a "$-$" in front of the square root) lead to a negative flow rate and is not considered in this analysis. An additional simplification is obtained by writing $A_3 \approx \omega_c^2 + \omega_d^2$, *i.e.* discarding the term which is multiplied by the small factor $\eta_c'\eta_d$. With this approximation, we obtain

$$A_4 \approx \frac{A_2}{2}\left(\omega_c^2 + \omega_d^2 + \sqrt{(\omega_c^2 - \omega_d^2)^2}\right) = A_2 \max(\omega_c^2, \omega_d^2) \tag{31}$$

Finally replacing A_4 we obtain a stability condition

- if $\omega_c > \omega_d$,

$$\frac{5Q_0}{2a_0}\,\frac{Z_0\gamma}{m\tau_c} \lesssim 2\eta_c'\omega_c(\omega_c^2 - \omega_d^2) \tag{32}$$

- if $\omega_d > \omega_c$,

$$\frac{5Q_0}{2a_0}\frac{Z_0\gamma}{m\tau_c} \lesssim 2\eta_d\omega_d(\omega_d^2 - \omega_c^2) \tag{33}$$

This approximate formula emphasizes the different conditions that influences the instability threshold. The instability occurs at lower flow rates for small damping, for matched eigenfrequency between the disk and the cavity and for a small response time of the cavity τ_c. Quantitatively the validity of this approximation is limited to small values of Q_0 (see 10) and thus cannot be used in practical design situations.

6. Conclusion

The instability of a deformable disc in an Axial Balancing System of a turbopump was demonstrated in a well controlled experiment. By matching the eigenfrequencies of an acoustic cavity and a deformable disk and by carefully controlling the inner valve geometry, we were able to trigger self-sustained oscillations. We emphasize here the efficiency of the resonant interactions that lead to significant oscillations of the rigid disk. We provide a complete characterization of the experimental system to allow for comparison with models or numerical simulations.

We propose a model to study the coupling between the axisymmetric modes of the disk and the cavity. The model is used to compute the critical flow rate at which the stationary state of the disk becomes unstable. The prediction of the model is compared with the critical flow rate determined in the experiment and it shows a very good agreement. These results attest the validity of our analytical interpretation that involves a competition between two coupled oscillators, the acoustic cavity and the disc, and emphasizes the role of the stiffness of the inner valve.

The model was validated for a specific range of pressure loss and flow condition. An exact formulation of the pressure loss through the inner valve may be used to extend the stability condition to a specific geometry of the Axial Balancing System. In addition a further improvement to the predictive aspect of the model would be to improve the model to allow for the determination of the damping of the disk.

Finally, it is worth noting that non-axisymmetric mode may also become unstable (at higher flow rates). Our analysis could be adapted to account for such cases but this is out of the scope of the present study.

The authors wish to acknowledge Giuseppe Fiore from the CNES (French space agency) and Martin Seive and David Testa from Ariane Group for scientific discussions during this research collaboration founded by the CNES under contract RT-CT-253-0000-1804-CNES.

Appendix A. Static solution for an annular disk with a uniform pressure drop across its faces

The solution for a disk clamped at αR (with $\alpha < 1$) and free at R with a uniform pressure difference ΔP applied to its faces reads

$$w(r) = \frac{\Delta P\, R^4}{64D}\left\{\frac{r^4}{R^4} - 8\frac{r^2}{R^2}\log\left(\frac{r}{R}\right) + K_1\frac{r^2}{R^2} + K_2\log\left(\frac{r}{R}\right) + K_3\right\}, \tag{A.1}$$

with

$$\begin{aligned}
K_1 &= 2\,\frac{-\alpha^4(1-\nu) + 2\alpha^2(1-\nu) + 4\alpha^2(1-\nu)\log(\alpha) + \nu + 3}{\alpha^2(1-\nu) + 1 + \nu},\\
K_2 &= 4\alpha^2\,\frac{-\alpha^2(\nu+1) + 4(\nu+1)\log(\alpha) - 1 + \nu}{\alpha^2(1-\nu) + 1 + \nu},\\
K_3 &= \alpha^2\,\frac{\alpha^4(1-\nu) + \alpha^2(3\nu-5) + 4\left[\alpha^2(\nu+1) + \nu + 3\right]\log(\alpha) - 16(\nu+1)\log^2(\alpha) + 2(\nu+3)}{\alpha^2(1-\nu) + 1 + \nu}
\end{aligned}$$

This form is compared with the measurements in Fig. 4.

Appendix B. Acoustic cavity

In this section, we propose a model to characterise the response of the acoustic cavity. Since the forcing and the viscous terms are neglected in the wave equation 6, the velocity field is irrotational and it is convenient to solve equation (6) using the velocity potential ψ defined as $\vec{v} = \vec{\nabla}\psi$. The acoustic equation then becomes

$$\frac{1}{c_0^2}\frac{\partial^2 \psi}{\partial t^2} - \Delta\psi = 0 \tag{B.1}$$

We consider that the geometry of the cavity is imposed *i.e.* we neglect the influence of the small displacement of the disc on the boundary condition at $z \approx 0$. The different boundary conditions for an harmonic perturbation write

$$\begin{aligned}
v_z(r, z = 0) &= 0 && \text{(B.2)}\\
v_r(r = R, z) &= -\hat{V}_Q \exp(-i\omega t) && \text{(B.3)}\\
v_r(r = 0, z) &= 0 && \text{(B.4)}\\
v_z(r, z = H) &= \hat{V}_x \mathcal{H}(r - R_x) \exp(-i\omega t) && \text{(B.5)}
\end{aligned}$$

where $\mathcal{H}(x) = 1$ if $x < 0$ and 0 otherwise. We assumed that the motion of the disc does not significantly modify the acoustic response of the cavity and therefore we enforce no motion at the contact with the disc. In addition we consider that the entry conditions result in a plug flow with a uniform radial velocity $\hat{V}_Q = \hat{Q}/(2\pi RH)$ and that the output of the cavity is also characterized by a plug flow with an harmonic exit flow rate $\hat{Q}_x \exp(-i\omega t)$ localised in $r \leq R_x$ with a velocity $\hat{V}_x = \hat{Q}_x/(\pi R_x^2)$ where R_x is the radius of the exit section.

Considering equation (B.1) in cylindrical coordinates and looking for the harmonic response, we can write it under the form of a Bessel equation [17, 18]. Considering only the axisymmetric modes, the solution writes

$$\psi = \sum_k \mathrm{J}_0(p_k r)\frac{1}{2}\left[A_k e^{q_k z} + B_k e^{-q_k z}\right] e^{-i\omega t} \tag{B.6}$$

with $p_k^2 = q_k^2 + (\omega/c_0)^2$, where q_k is the wave number in the axial direction z. The p_k's form a discrete set imposed by the boundary conditions as shown below. J_0 is the zero order Bessel function of the first kind, and the magnitudes A_k and B_k are to be determined with the boundary conditions.

In the specific radial and axial directions, the velocities v_r and v_z are obtained from the derivative of ψ in r and z respectively. Equation B.2 yields $B_k = A_k$ leading to

$$v_r = \sum_k -p_k\, \mathrm{J}_1(p_k r) A_k \cosh(q_k z) e^{-i\omega t} \tag{B.7}$$

$$v_z = \sum_k q_k\, \mathrm{J}_0(p_k r) A_k \sinh(q_k z) e^{-i\omega t} \tag{B.8}$$

To enforce the boundary condition B.3 we write the solution for v_r under the form

$$v_r = \left\{ -p_0 A_0' J_1(p_0 r) + \sum_{k=1}^{\infty} -p_k\, \mathrm{J}_1(p_k r) A_k \cosh(q_k z) \right\} e^{-i\omega t} \tag{B.9}$$

with $A_0' = \hat{V}_Q/[p_0 J_1(p_0 R)]$ and $p_0 = \omega/c_0$. For all other modes, the p_k form a discrete set of values verifying $\mathrm{J}_1(p_k R) = 0$ for $k = 1, 2, \cdots$. The equation $J_1(\lambda) = 0$ has an infinity of discrete solutions λ_k, the zeros of the Bessel function J_1. The general solution then writes,

$$\psi = \left\{ A_0' J_0(p_0 r) + A_0 \cosh(q_0 z) + \sum_{k=1}^{\infty} \mathrm{J}_0(p_k r) A_k \cosh(q_k z) \right\} e^{-i\omega t} \tag{B.10}$$

with $q_0 = i(\omega/c_0)$.

We now impose the condition B.5. We consider a harmonic output flow rate $\hat{Q}_x \exp(-i\omega t)$ resulting in $v_z = \hat{V}_x \exp(-i\omega t)$ for $r < R_x$ and $v_z = 0$ otherwise, with $\hat{V}_x = \hat{Q}_x/(\pi R_x^2)$

The coefficients A_k can be determined by using the relation

$$\int_0^R r\,\mathrm{J}_0(p_k r)\,\mathrm{J}_0(p_{k'} r)\,\mathrm{d}r = \frac{1}{2} R^2 J_0^2(p_k R)\delta(k-k') \tag{B.11}$$

that holds because $\mathrm{J}_1[p_k R] = 0$ (see *e.g.* [19]) and one obtains for $k = 1, 2, ...$

$$A_k = \hat{V}_x \frac{2R_x J_1(p_k R_x)}{p_k q_k R^2 J_0^2(p_k R)\sinh(q_k H)} \tag{B.12}$$

and

$$A_0 = \hat{V}_x \frac{R_x^2}{q_0 R^2 \sinh(q_0 H)} \tag{B.13}$$

The pressure field in the cavity that couples with the vibration of the disk can then be obtained through the relation $P_c = -\rho_0 \partial\Psi/\partial t$ in $z = 0$.

In the following, the non dimensional quantities will be used

$$\tilde{\omega} = \frac{\omega c_0}{R}, \quad \eta = \frac{H}{R}, \quad \sigma = \frac{R_x}{R} \tag{B.14}$$

together with the variables $\tilde{r} = r/R$ and $\tilde{z} = z/H$ and the solution for the velocity potential can be written

$$\psi = \left\{ \frac{\hat{Q}}{\pi R}\tilde{A}_0' J_0(\tilde{p_0}\tilde{r}) + \frac{\hat{Q}_x}{\pi R}\tilde{A}_0 \cosh(\tilde{q_0}\tilde{z}) + \frac{\hat{Q}_x}{\pi R}\sum_{k=1}^{\infty} \tilde{A}_k\,\mathrm{J}_0(\tilde{p_k}\tilde{r})\cosh(\tilde{q_k}\tilde{z}) \right\} e^{-i\omega t} \tag{B.15}$$

$$\tilde{p}_0 = \tilde{\omega}, \quad \tilde{q}_0 = i\eta\tilde{\omega}, \quad \tilde{p}_k = \lambda_k, \quad \tilde{q}_k = \eta\sqrt{\lambda_k^2 - \tilde{\omega}^2} \tag{B.16}$$

where λ_k is a zero of the J_1 Bessel function and

$$\tilde{A}_0' = \frac{1}{2\eta\tilde{p}_0 J_1(\tilde{p}_0)}, \quad \tilde{A}_0 = \frac{\eta}{\tilde{q}_0 \sinh(\tilde{q}_0)}, \quad \tilde{A}_k = \frac{2\eta J_1(\tilde{p}_k\sigma)}{\sigma\tilde{p}_k\tilde{q}_k \sinh(\tilde{q}_k) J_0^2(\tilde{p}_k)}, \tag{B.17}$$

The acoustic field depends on the exit flow rate $\hat{Q}_x$ that is not known *a priori*. We consider that the exit conditions are those of a massless piston, thus assuming a homogeneous exit velocity. Computing the impedance associated with such condition is a classical problem of acoustics (see e.g. [20]) and the impedance can be written

$$Z_x = \frac{\hat{P}_x}{\hat{Q}_x} = \frac{\rho_0 c_0}{\pi R_x^2}(a_x - ib_x) = Z_0 \frac{1}{\sigma^2}(a_x - ib_x) \tag{B.18}$$

with, for R_x small compared with the wavelength,

$$a_x = \frac{1}{2}\left(\frac{\omega R_x}{c}\right)^2 = \frac{1}{2}\left(\frac{\tilde{\omega}}{\sigma}\right)^2 \quad \text{and} \quad b_x = \frac{8}{3\pi}\left(\frac{\omega R_x}{c}\right) = \frac{8}{3\pi}\left(\frac{\tilde{\omega}}{\sigma}\right)$$

Here, the characteristic impedance of the cavity is $Z_0 = (\rho_0 c_0)/(\pi R^2)$.

To address the dynamics of the system the impedance Z_e in $r = R$ should be computed. Since the acoustics has been computed with an exit flow rate Q_x one can use the two formal relationship

$$P_x = iZ_0(\alpha_x Q + \beta_x Q_x) \tag{B.19}$$

$$P_R = iZ_0(\alpha_e Q + \beta_e Q_x) \tag{B.20}$$

In these equations, P_x is the (mean) pressure at the exit section ($r \leq R_x, z = H$) and the coefficients α_x and β_x can be computed using Eq. (B.10)

$$\alpha_x = \tilde{\omega}\tilde{A}_0' \frac{2J_1(\tilde{p}_0\sigma)}{\tilde{p}_0\sigma} \tag{B.21}$$

$$\beta_x = \tilde{\omega}\left\{\tilde{A}_0 \cosh(\tilde{q}_0\eta) + \sum_{k=1}^{\infty} \tilde{A}_k \cosh(\tilde{q}_k\eta)\frac{2J_1(\tilde{p}_k\sigma)}{\tilde{p}_k\sigma}\right\} \tag{B.22}$$

P_R is the pressure at the entry section ($r = R, z = 0$), and, using Eq. (B.10),

$$\alpha_e = \tilde{\omega}\tilde{A}_0' J_0(\tilde{p}_0) \tag{B.23}$$

$$\beta_e = \tilde{\omega}\left\{\tilde{A}_0 + \sum_{k=1}^{\infty} \tilde{A}_k J_0(\tilde{p}_k)\right\} \tag{B.24}$$

Combining eqns. (B.19) and (B.20) with eq. (B.18) yields

$$Z_e = \frac{P_R}{Q} = Z_0\left(i\alpha_e - \beta_e \frac{\alpha_x}{Z_x/Z_0 - i\beta_x}\right) \tag{B.25}$$

The different coefficients α and β can be computed by performing the summation numerically for a given set of parameters. The quantity of interest is Z_e. It depends on the geometry (*i.e.* the parameters η and σ) and Z_0. To make the analysis more concrete, we plot the input impedance for a set of parameters related to the experimental setup in Figure B.11.

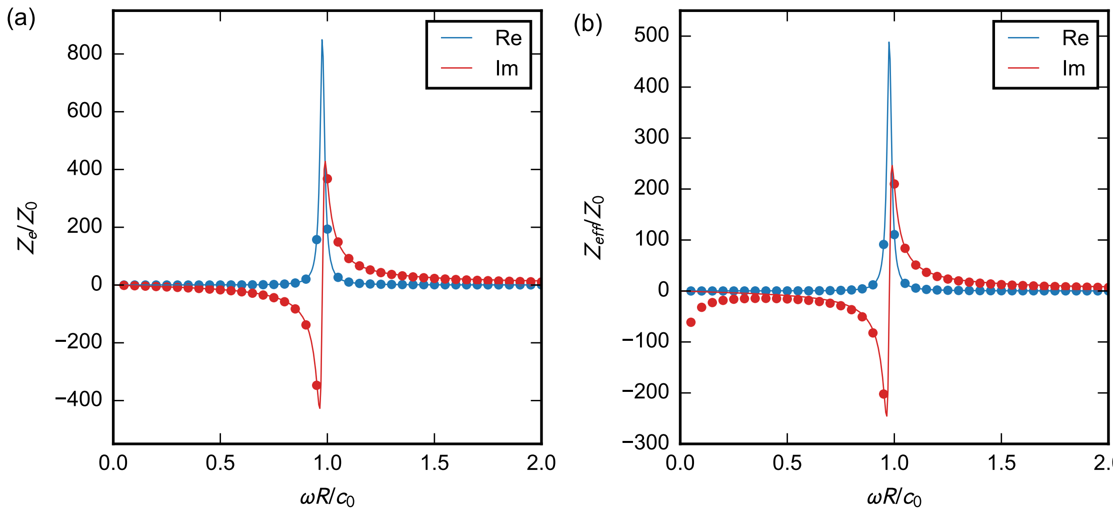

Figure B.11: Non dimensional input impedance Z_e/Z_0 and effective impedance Z_{eff}/Z_0 for $R = 90$ mm, $H = 5$ mm, $R_x = 14.1$ mm. The dots show the real and imaginary parts obtained by computing the sums with 300 modes. The continuous lines show the approximation by a resonator (eq. B.26) with $\omega_c = 0.976\ c_0/R$, $\eta_c = 0.0129$, $\tau_c = 0.0461\ R/c_0$ and $\gamma = 0.575$.

To perform the stability analysis of the whole system, a simplified form is useful. We note that the dynamics of the cavity near its first resonance is well approximated by a damped resonator of the form

$$Z_e = Z_0 \frac{-i\omega/\tau_c}{\omega_c^2 - \omega^2 - 2i\eta_c\omega_c\omega} \tag{B.26}$$

where τ_c is a typical time scale of the cavity, ω_c is the frequency of the first resonance of te cavity and η_c is a damping coefficient associated with acoustic radiation through the exit orifice.

Finally, it is worth noting that a similar computation can be performed for the effective pressure P_{eff} (the equivalent pressure acting on the disk)

$$P_{eff} = \frac{1}{\pi R^2} \int_0^R 2\pi r P(r, z=0, t) \left(\frac{r}{R}\right)^2 dr \tag{B.27}$$

Similar results can be found and in particular, we obtain that in the regime of interest, the effective pressure can be written $P_{eff} = \gamma P_R$.

To make the simplified more quantitative, we use the different geometrical parameters of the experiment and notably the value $R_x = 14.1$ mm that was determined by using the relation $\pi R_x^2 = S_x$ where S_x is the total area of the exit orifices. With these values we obtain (see also Fig. B.11)

$$\tau_c = \frac{R}{c_0} 0.0461105, \quad \omega_c = \frac{c0}{R} 0.976313, \quad \eta_c = 0.0129, \quad \gamma = 0.5749 \tag{B.28}$$

Appendix C. Stability criterion

In the marginally stable state, when a pair of eigenvalues have a zero real part, the characteristic polynomial can be written

$$(s - a_1 + ib_1)(s - a_1 - ib_1)(s + ib_2)(s - ib_2) = 0 \tag{C.1}$$

When expanding and identifying with the form 27 one obtains

$$A_2 = -2a_1, \quad A_3 = a_1^2 + b_1^2 + b_2^2, \quad A_4 = -2a_1 b_2^2, \quad A_5 = b_2^2(a_1^1 + b_1^2) \tag{C.2}$$

To obtain a solution of this set of equations, a necessary condition is

$$A_2 A_3 A_4 - A_4^2 - A_5 A_2^2 = 0 \tag{C.3}$$

Therefore, this equation acts as a stability boundary.

References

[1] T. Young, T. Shiau, Z. Kuo, Dynamic stability of rotor-bearing systems subjected to random axial forces, Journal of sound and vibration 305 (3) (2007) 467–480.

[2] J. M. Reddecliff, J. H. Vohr, Hydrostatic bearings for cryogenic rocket engine turbopumps, Journal of Lubrication Technology 91(3) (1969) 557–575.

[3] T. Shimura, S. Kawasaki, M. Uchiumi, T. Kimura, M. Hayashi, J. Matsui, Stability of an axial thrust self-balancing system, Journal of fluids engineering 135 (1) (2013).

[4] G. Verhille, P. Le Gal, Couplage d'oscillateurs : l'instabilité d'un système d'équilibrage axial d'une turbo-pompe, 23ème Congrès Français de Mécanique (2017).

[5] G. Verhille, P. Le Gal, Oscillators coupling: The instability of an axial equilibrium system of a turbo-pump, 16TH European Turbulence Conference, Stockholm (Sweden) (21-24 AUGUST 2017).

[6] C. D'Angelo, III, C. D. Mote, Aerodynamically excited vibration and flutter of a thin disk rotating at supercritical speed, Journal of Sound and Vibration 168 (1) (1993) 15–30.

[7] B. C. Kim, A. Raman, C. D. Mote, Jr., Prediction Of Aeroelastic Flutter In A Hard Disk Drive, Journal of Sound and Vibration 238 (2) (2000) 309–325.

[8] D. Capdevila, Capcom espace, le moteur vulcain 2 (1999).
URL http://www.capcomespace.net/dossiers/espace_europeen/ariane/ariane5/moteur_vulcain2.htm

[9] A. W. Leissa, Vibration of plates, NASA, Washington D.C., 1969.

[10] P. Cawley, N. Sarsentis, A quick metthod for the measurement of structural damping, Mechanical systems and signal processing 2 (1) (39–47 1988).

[11] S. Timoshenko, S. Woinowsky-Krieger, Theoy of Plates and Shells, McGraw-Hill, 1959.

[12] I. E. Idelc'hik, Handbook of hydraulic resistance, 3rd Edition, Jaico Publishing, 2003.

[13] T. A. Wilson, G. S. Beavers, Operating modes of the clarinet, Journal of the Acousticical Society of America 56 (2) (1974) 653 – 658.
[14] N. H. Fletcher, T. D. Rossing, The Physics of Musical Instruments, 2nd Edition, Springer, New York, 1998.
[15] L. Landau, E. Lifchitz, Théorie de l'élasticité, Tome 7, 2ème édition, MIR, Moscow, 1990.
[16] A. W. Leissa, The historical bases of the Rayleigh and Ritz methods, Journal of Sound and Vibration 287 (4-5) (2005) 961–978.
[17] G. N. Watson, Theory of Bessel Functions, Cambridge University Press, Cambridge, 1945.
[18] G. Dattoli, T. Amalia, Theory and applications of generalized Bessel functions, ARACNE Ed., Roma, 1996.
[19] I. N. Sneddon, Special functions of mathematical physics and chemistry, Oliver and Boyd, 1956.
[20] L. Rayleigh, The theory of Sound, McMillan, New York, 1894.
[21] Q. Ni, Y. Luo, M. Li, H. Yan, Natural frequency and stability analysis of a pipe conveying fluid with axially moving supports immersed in fluid, Journal of Sound and Vibration 403 (2017) 173–189.